RADIO SCIENCE, VOL. 42, RS6S16, doi:10.1029/2007RS003663, 2007

Analytical and numerical investigation of the radiation from concentric metamaterial spheres excited by an electric Hertzian dipole

Samel Arslanagic,[1] Richard W. Ziolkowski,[2] and Olav Breinbjerg[1]

Received 19 March 2007; revised 20 July 2007; accepted 6 August 2007; published 19 October 2007.

[1] The canonical problem of an electric Hertzian dipole radiating in the presence of a pair of concentric double negative metamaterial spheres is investigated analytically and numerically. The spatial distribution of the near field as well as the total radiated power are examined. The results are compared to those for the corresponding structures made of conventional double positive materials. It is shown that electrically small concentric metamaterial spheres can be designed to be resonant and that these resonant designs lead to significant changes in the field radiated by the electric Hertzian dipole and, in particular, to significant enhancements of the total power radiated by it. The impact of the location of the electric Hertzian dipole in both radiating and scattering configurations is studied in detail. Furthermore, the influence of dispersion and loss is investigated. Finally, a few results for larger size metamaterial concentric spheres are given.

Citation: Arslanagic, S., R. W. Ziolkowski, and O. Breinbjerg (2007), Analytical and numerical investigation of the radiation from concentric metamaterial spheres excited by an electric Hertzian dipole, *Radio Sci.*, *42*, RS6S16, doi:10.1029/2007RS003663.

1. Introduction

[2] Recent years have witnessed an increased interest in various classes of metamaterials (MTMs), such as double-negative (DNG) and single-negative (SNG) materials, as well as combinations of these with conventional double-positive (DPS) materials. A significant amount of work has already been performed on fundamental issues as well as potential applications [see, e.g., *Caloz and Itoh*, 2006; *Eleftheriades and Balmain*, 2005; *Engheta and Ziolkowski*, 2006, and references therein].

[3] The increased interest in MTMs is mainly due to the unusual properties of DNG materials [*Veselago*, 1968] which are characterized by a negative real part of the permittivity as well as the permeability. These unusual properties are not present in conventional DPS materials which are characterized by a positive real part of those parameters. In particular, the concept of the so-called perfect lens [*Pendry*, 2000], consisting of a specific DNG slab, has attracted much attention. Moreover, combinations of DNG and DPS materials have lead to a new paradigm in the miniaturization of devices such as cavity resonators [*Engheta*, 2002], waveguides [*Alú and Engheta*, 2004], scatterers [*Alú and Engheta*, 2005; *Arslanagic et al.*, 2006], and antennas [*Alú et al.*, 2007; *Arslanagic et al.*, 2006; *Stuart and Pidwerbetsky*, 2006; *Ziolkowski and Erentok*, 2006; *Ziolkowski and Kipple*, 2003, 2005]. Many of these ideas were based on the observed properties of such electrically small MTM-based structures when illuminated by plane waves or by localized sources such as an electric Hertzian dipole (EHD) or an electric line source (ELS). In particular, it has been observed that such electrically small MTM-based structures can be designed to be resonant and that these resonant designs lead to significant enhancements of the total radiated power or the total scattering cross section. This is in contrast to electrically small structures made of only conventional DPS materials.

[4] The purpose of this work is to further investigate the radiation properties of electrically small spherical MTM-based structures that are excited by an arbitrarily oriented and located EHD. In extension of the works of *Ziolkowski and Kipple* [2003, 2005], where the EHD is located at the origin, the present work investigates also other EHD locations and documents the

[1]Ørsted·DTU, ElectroScience Section, Technical University of Denmark, Lyngby, Denmark.
[2]Department of Electrical and Computer Engineering, University of Arizona, Tucson, Arizona, USA.

0048-6604/07/2007RS003663$11.00

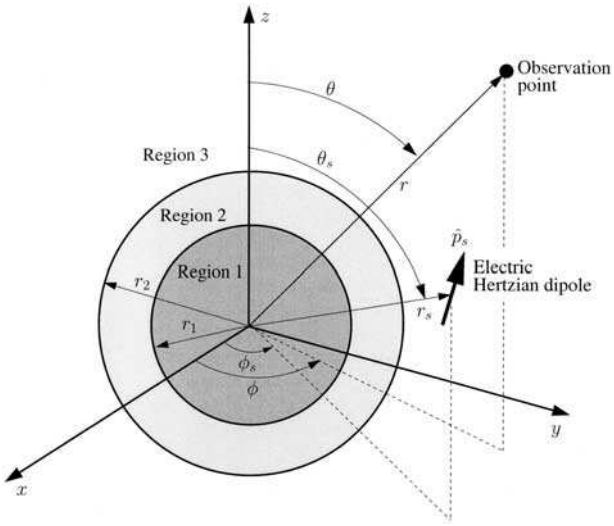

Figure 1. Configuration of the EHD-excited concentric pair of MTM spheres.

properties and advantages of such configurations. In particular, it is shown that these structures remain resonant independent of the source location or orientation and that they still lead to significant enhancements of the total radiated power as compared to the power radiated by the EHD in free space. It is emphasized that the present investigation is entirely theoretical as it assumes the existence of electrically small DNG materials and considers a canonical configuration with an impressed Hertzian dipole source.

[5] The present manuscript is organized as follows. In section 2, the analytical solution is derived for the problem of an arbitrarily located and oriented EHD radiating in the presence of a pair of concentric MTM spheres. This section also defines quantities which are used in subsequent numerical investigations of these structures. The condition for resonance in the electrically small designs is derived and discussed in section 3, while section 4 presents a detailed numerical investigation of the near-field spatial distribution and the total radiated power of these designs. Two types of structures, referred to as the dipolar and quadrupolar ones, are studied in section 4. The influence of dispersion and loss, present in any realistic MTM, is taken into account in section 5, while the properties of structures having larger electrical sizes are discussed in section 6. The potential use of SNG materials in similar electrically small designs is clarified in section 7. The entire work is summarized and concluded in section 8. Throughout this manuscript, the time factor $\exp(j\omega t)$ with ω being the angular frequency, and t being the time, is assumed and suppressed.

2. Analytical Solution

2.1. Configuration

[6] The configuration of interest is depicted in Figure 1. A sphere (region 1) of radius r_1 is covered with a concentric spherical shell of radius r_2 (region 2) and immersed in an infinite ambient medium (region 3). The concentric MTM spheres are illuminated by an EHD possessing the dipole moment $\vec{p}_s = \hat{p}_s\, p_s$ with the orientation $\hat{p}_s$ and complex magnitude p_s [Am]. The EHD can be located in any of the three regions and can possess an arbitrary orientation and complex magnitude of the dipole moment. The EHD constitutes a model of an electrically short dipole with p_s being the product of the current and length of that dipole. Region i, with $i = 1$ and 2, is characterized by a permittivity and a permeability, denoted by $\varepsilon_i = \varepsilon_i' - j\varepsilon_i''$ and $\mu_i = \mu_i' - j\mu_i''$, respectively, while the wave number inside region i is $k_i = \omega\sqrt{\varepsilon_i\mu_i}$, where the branch of the square root is chosen such that $\mathrm{Im}\{k_i\} \leq 0$. Both region 1 and 2 can be composed of simple DPS, DNG, and/or SNG materials. The exterior region, region 3, is free space with the permittivity ε_0 and permeability μ_0. Thus, its wave number is $k_0 = \omega\sqrt{\varepsilon_0\mu_0}$ and intrinsic impedance $\eta_0 = \sqrt{\mu_0/\varepsilon_0}$. A spherical coordinate system (r, θ, ϕ) and the associated Cartesian coordinate system (x, y, z) are introduced such that the origin coincides with the common center of the spheres. The coordinates of the observation point and the EHD are (r, θ, ϕ) and (r_s, θ_s, ϕ_s), respectively.

2.2. Field of the EHD

[7] Following the approach of *Jones* [1965, chapter 8], the electric field generated by the EHD in an infinite medium, characterized by $\varepsilon_{\mathrm{EHD}}$, μ_{EHD}, and k_{EHD}, can be expressed as an expansion of spherical transverse magnetic (TM) and transverse electric (TE) waves

$$\begin{Bmatrix} \vec{E}_{\mathrm{EHD}}(r,\theta,\phi) \\ \vec{H}_{\mathrm{EHD}}(r,\theta,\phi) \end{Bmatrix} = \sum_{n=1}^{N_{\max}} \sum_{m=-n}^{n} \left[\frac{1}{j\omega\varepsilon_{\mathrm{EHD}}\mu_{\mathrm{EHD}}} \begin{Bmatrix} a_{nm}^{(c)}\vec{N}_{nm}^{(\mathrm{TM}),(c)} \\ b_{nm}^{(c)}\vec{N}_{nm}^{(\mathrm{TE}),(c)} \end{Bmatrix} + \begin{Bmatrix} (-1/\varepsilon_{\mathrm{EHD}})b_{nm}^{(c)}\vec{M}_{nm}^{(\mathrm{TE}),(c)} \\ (1/\mu_{\mathrm{EHD}})a_{nm}^{(c)}\vec{M}_{nm}^{(\mathrm{TM}),(c)} \end{Bmatrix} \right], \quad (1)$$

where the familiar spherical vector wave functions (SVWFs) are

$$\vec{M}_{nm}^{(\Gamma),(c)}(r,\theta,\phi) = \gamma_{\mathrm{EHD}} w_n^{(c)}(k_{\mathrm{EHD}} r) e^{jm\phi} \cdot \left[\frac{jm}{\sin\theta} P_n^{|m|}(\cos\theta)\hat{\theta} - \frac{d}{d\theta} P_n^{|m|}(\cos\theta)\hat{\phi} \right], \tag{2}$$

$$\vec{N}_{nm}^{(\Gamma),(c)}(r,\theta,\phi) = \gamma_{\mathrm{EHD}} \frac{n(n+1)}{r} w_n^{(c)}(k_{\mathrm{EHD}} r) P_n^{|m|}(\cos\theta) \cdot e^{jm\phi}\hat{r} + \gamma_{\mathrm{EHD}} \frac{1}{r}\frac{d}{dr}\{r w_n^{(c)}(k_{\mathrm{EHD}} r)\} \cdot \frac{d}{d\theta} P_n^{|m|}(\cos\theta) e^{jm\phi}\hat{\theta} + \gamma_{\mathrm{EHD}} \frac{1}{r}\frac{d}{dr} \cdot \{r w_n^{(c)}(k_{\mathrm{EHD}} r)\} \frac{jm}{\sin\theta} P_n^{|m|}(\cos\theta) e^{jm\phi}\hat{\phi}, \tag{3}$$

with $\gamma_{\mathrm{EHD}} = \varepsilon_{\mathrm{EHD}}$ for Γ = TE, and $\gamma_{\mathrm{EHD}} = \mu_{\mathrm{EHD}}$ for Γ = TM, and with $w_n^{(c)}(\cdot)$ being a specific spherical function to be introduced below. The quantities $a_{nm}^{(c)}$ and $b_{nm}^{(c)}$ are the TM and TE expansion coefficients, respectively, of the EHD field which can be expressed as

$$a_{nm}^{(c)} = -jk_{\mathrm{EHD}} \frac{p_s}{4\pi} \frac{1}{\mu_{\mathrm{EHD}}} \frac{2n+1}{n(n+1)} \frac{(n-|m|)!}{(n+|m|)!} \cdot \left\{ \hat{p}_s \cdot \vec{N}_{n,-m}^{(\mathrm{TM}),(5-c)}(r_s,\theta_s,\phi_s) \right\}, \tag{4}$$

and

$$b_{nm}^{(c)} = \frac{k_{\mathrm{EHD}}^3}{\omega} \frac{p_s}{4\pi} \frac{1}{\varepsilon_{\mathrm{EHD}}^2} \frac{2n+1}{n(n+1)} \frac{(n-|m|)!}{(n+|m|)!} \cdot \left\{ \hat{p}_s \cdot \vec{M}_{n,-m}^{(\mathrm{TE}),(5-c)}(r_s,\theta_s,\phi_s) \right\}. \tag{5}$$

[8] For $r < r_s$ c is equal to 1, and for $r > r_s$ c is equal to 4. The function $w_n^{(1)}(\cdot) = j_n(\cdot)$, where $j_n(\cdot)$ is the spherical Bessel function of order n, is chosen to represent the field for $r < r_s$ due to its nonsingular behavior at the origin, while $w_n^{(4)}(\cdot) = h_n^{(2)}(\cdot)$, $h_n^{(2)}(\cdot)$ being the spherical Hankel function of second kind and order n, is chosen for $r > r_s$ because it represents an outward propagating wave complying with the radiation condition. The function $P_n^{|m|}$ is the associated Legendre function of the first kind of degree n and order $|m|$. The symbol $N_{\max}$ is the truncation limit in a practical numerical implementation of the infinite summation in the exact solution and is chosen in a manner that ensures the convergence of this expansion. When the EHD is located in regions 1 and 2, $\varepsilon_{\mathrm{EHD}} = \varepsilon_i$, $\mu_{\mathrm{EHD}} = \mu_i$, and $k_{\mathrm{EHD}} = k_{\mathrm{i}}$, for i = 1 and 2, respectively, while $\varepsilon_{\mathrm{EHD}} = \varepsilon_0$, $\mu_{\mathrm{EHD}} = \mu_0$, and $k_{\mathrm{EHD}} = k_0$ when the EHD is in region 3.

2.3. Unknown Fields

[9] The unknown fields in each of the three regions, i.e., the scattered field in the region containing the EHD and the total fields in the other regions, are likewise expanded in terms of SVWFs. Therefore, these can be expressed as

$$\begin{Bmatrix} \vec{E}_{1s}(r,\theta,\phi) \\ \vec{H}_{1s}(r,\theta,\phi) \end{Bmatrix} = \sum_{n=1}^{N_{\max}} \sum_{m=-n}^{n} \left[\frac{1}{j\omega\varepsilon_1\mu_1} \begin{Bmatrix} A_{1,nm}\vec{N}_{nm}^{(\mathrm{TM}),(1)} \\ B_{1,nm}\vec{N}_{nm}^{(\mathrm{TE}),(1)} \end{Bmatrix} + \begin{Bmatrix} (-1/\varepsilon_1)B_{1,nm}\vec{M}_{nm}^{(\mathrm{TE}),(1)} \\ (1/\mu_1)A_{1,nm}\vec{M}_{nm}^{(\mathrm{TM}),(1)} \end{Bmatrix} \right] \quad \text{for } r \le r_1, \tag{6a}$$

$$\begin{Bmatrix} \vec{E}_{2s}(r,\theta,\phi) \\ \vec{H}_{2s}(r,\theta,\phi) \end{Bmatrix} = \sum_{n=1}^{N_{\max}} \sum_{m=-n}^{n} \left[\frac{1}{j\omega\varepsilon_2\mu_2} \begin{Bmatrix} A_{2,nm}\vec{N}_{nm}^{(\mathrm{TM}),(1)} + A_{3,nm}\vec{N}_{nm}^{(\mathrm{TM}),(2)} \\ B_{2,nm}\vec{N}_{nm}^{(\mathrm{TE}),(1)} + B_{3,nm}\vec{N}_{nm}^{(\mathrm{TE}),(2)} \end{Bmatrix} + \begin{Bmatrix} (-1/\varepsilon_2)\left(B_{2,nm}\vec{M}_{nm}^{(\mathrm{TE}),(1)} + B_{3,nm}\vec{M}_{nm}^{(\mathrm{TE}),(2)}\right) \\ (1/\mu_2)\left(A_{2,nm}\vec{N}_{nm}^{(\mathrm{TM}),(1)} + A_{3,nm}\vec{N}_{nm}^{(\mathrm{TM}),(2)}\right) \end{Bmatrix} \right] \quad \text{for } r_1 \le r \le r_2, \tag{6b}$$

$$\begin{Bmatrix} \vec{E}_{3s}(r,\theta,\phi) \\ \vec{H}_{3s}(r,\theta,\phi) \end{Bmatrix} = \sum_{n=1}^{N_{\max}} \sum_{m=-n}^{n} \left[\frac{1}{j\omega\varepsilon_0\mu_0} \begin{Bmatrix} A_{4,nm}\vec{N}_{nm}^{(\mathrm{TM}),(4)} \\ B_{4,nm}\vec{N}_{nm}^{(\mathrm{TE}),(4)} \end{Bmatrix} + \begin{Bmatrix} (-1/\varepsilon_0)B_{4,nm}\vec{M}_{nm}^{(\mathrm{TE}),(4)} \\ (1/\mu_0)A_{4,nm}\vec{M}_{nm}^{(\mathrm{TM}),(4)} \end{Bmatrix} \right] \quad \text{for } r \ge r_2, \tag{6c}$$

where $A_{i,nm}$, i = 1,. . ., 4 are the unknown expansion coefficients associated with the TM part of the fields and, henceforth, are referred to as the TM coefficients, while $B_{i,nm}$, i = 1,. . ., 4 are the unknown expansion coefficients associated with the TE part of the fields and, henceforth, are referred to as the TE coefficients. It is noted that the expansion in (6b) also contains the function $w_n^{(2)}(\cdot) = y_n(\cdot)$, where $y_n(\cdot)$ is the spherical Neumann function of order n. The expressions (1) and (6a)–(6c) represent multipole expansions of the respective fields, i.e., the n = 1 term (for which $m = -1$, 0, and 1) corresponds to the dipolar mode, the n = 2 term (for which $m = -2, -1, 1, 2$) corresponds to the quadrupolar mode, and similarly for the other terms.

Table 1. Elements $\Psi_{i,nm}$, $i = 1, \ldots, 8$ of the Excitation Vector $\vec{\Psi}_{nm}$ When the EHD is Located in Regions 1, 2, or 3

$\Psi_{i,nm}$	EHD in Region 1	EHD in Region 2	EHD in Region 3
$\Psi_{1,nm}$	$-a_{nm}^{(4)} h_n^{(2)}(k_1 r_1)$	$a_{nm}^{(1)} j_n(k_2 r_1)$	0
$\Psi_{2,nm}$	$-a_{nm}^{(4)} d'_{r=r_1}\{r h_n^{(2)}(k_1 r)\}$	$(\varepsilon_1/\varepsilon_2) a_{nm}^{(1)} d'_{r=r_1}\{r j_n(k_2 r)\}$	0
$\Psi_{3,nm}$	0	$-a_{nm}^{(4)} h_n^{(2)}(k_2 r_2)$	$a_{nm}^{(1)} j_n(k_0 r_2)$
$\Psi_{4,nm}$	0	$-a_{nm}^{(4)} d'_{r=r_2}\{r h_n^{(2)}(k_2 r)\}$	$(\varepsilon_2/\varepsilon_0) a_{nm}^{(1)} d'_{r=r2}\{r j_n(k_0 r)\}$
$\Psi_{5,nm}$	$-b_{nm}^{(4)} h_n^{(2)}(k_1 r_1)$	$b_{nm}^{(1)} j_n(k_2 r_1)$	0
$\Psi_{6,nm}$	$-b_{nm}^{(4)} d'_{r=r_1}\{r h_n^{(2)}(k_1 r)\}$	$(\mu_1/\mu_2) b_{nm}^{(1)} d'_{r=r_1}\{r j_n(k_2 r)\}$	0
$\Psi_{7,nm}$	0	$-b_{nm}^{(4)} h_n^{(2)}(k_2 r_2)$	$b_{nm}^{(1)} j_n(k_0 r_2)$
$\Psi_{8,nm}$	0	$-b_{nm}^{(4)} d'_{r=r_2}\{r h_n^{(2)}(k_2 r)\}$	$(\mu_2/\mu_0) a_{nm}^{(1)} d'_{r=r_2}\{r j_n(k_0 r)\}$

[10] Enforcing the electromagnetic field boundary conditions, i.e., the continuity of the tangential components of the electric and magnetic fields at the interfaces $r = r_1$ and $r = r_2$, it can be shown that the unknown expansion coefficients are found from the following matrix relation

$$\vec{D}_{nm} = \left(\bar{\bar{S}}_n\right)^{-1} \vec{\Psi}_{nm}, \qquad n = 1, 2, \ldots N_{\max} \quad \text{and} \quad m = -n, \ldots, n \tag{7}$$

where $\vec{D}_{nm} = [A_{1,nm}, \ldots, A_{4,nm}, B_{1,nm}, \ldots, B_{4,nm}]$ is the vector containing the eight unknown expansion coefficients, and $\vec{\Psi}_{nm} = [\Psi_{1,nm}, \ldots, \Psi_{8,nm}]$ is the excitation vector which depends on the location of the EHD. The elements of this excitation vector, when the EHD is located in regions 1, 2 or 3, are shown in Table 1.

[11] In Table 1, as well as in certain forthcoming relations, use is made of the expression

$$d'_{r=r_k}\left\{r_k w_n^{(c)}(k_i r_k)\right\} = w_n^{(c)}(k_i r_k) + k_i r_k w_n^{(c)\prime}(k_i r_k), \tag{8}$$

where $w_n^{(c)\prime}(x) = dw_n^{(c)}(x)/dx$. The matrix $\bar{\bar{S}}_n$ is an eight-by-eight matrix that depends on the values of the SVWFs at the two interfaces. The explicit form of this matrix is given by

$$\bar{\bar{S}}_n = \begin{bmatrix} \bar{\bar{A}}_n & \bar{\bar{0}} \\ \bar{\bar{0}} & \bar{\bar{B}}_n \end{bmatrix}, \tag{9}$$

where $\bar{\bar{0}}$ is a four-by-four zero matrix, $\bar{\bar{A}}_n = \bar{\bar{\Gamma}}_n$ ($\gamma_i = \varepsilon_i$, $i = 1, 2$; $\gamma_3 = \varepsilon_0$) and $\bar{\bar{B}}_n = \bar{\bar{\Gamma}}_n$ ($\gamma_i = \mu_i$, $i = 1, 2$; $\gamma_3 = \mu_0$), with the matrix $\bar{\bar{\Gamma}}_n$ having the form of

$$\bar{\bar{\Gamma}}_n = \begin{bmatrix} j_n(k_1 r_1) & j_n(k_2 r_1) & -y_n(k_2 r_1) & 0 \\ d'_{r=r_1}\{r j_n(k_1 r)\} & -\frac{\gamma_1}{\gamma_2} d'_{r=r_1}\{r j_n(k_2 r)\} & -\frac{\gamma_1}{\gamma_2} d'_{r=r_1}\{r y_n(k_2 r)\} & 0 \\ 0 & j_n(k_2 r_2) & y_n(k_2 r_2) & -h_n^{(2)}(k_0 r_2) \\ 0 & d'_{r=r_2}\{r j_n(k_2 r)\} & d'_{r=r_2}\{r y_n(k_2 r)\} & -\frac{\gamma_2}{\gamma_3} d'_{r=r_2}\left\{r h_n^{(2)}(k_0 r)\right\} \end{bmatrix}. \tag{10}$$

[12] It is interesting to note that the first four elements of the excitation vector $\vec{\Psi}_{nm}$, i.e., $\Psi_{i,nm}$ with $i = 1, 2, 3$, and 4, see Table 1, are used only in the determination of the unknown TM coefficients $A_{i,nm}$, while the last four elements of this vector, i.e., $\Psi_{i,nm}$ with $i = 5, 6, 7$, and 8, are used in the determination of the unknown TE coefficients $B_{i,nm}$. This matrix structure is due to the fact that the TM and TE spherical modes are linearly independent and, hence, their coefficients are uncoupled. In other words, the linear system of equations used to determine the unknown TM coefficients, and the one used to determine the unknown TE coefficients, and vice versa, are uncoupled. As a consequence, relation (7) is split into two relations for numerical convenience, each involving a four-by-four matrix of the form given by (10) to determine the $A_{i,nm}$ on the one hand, and $B_{i,nm}$ on the other. This fact will also be used in section 3 in order to obtain the conditions for resonance.

2.4. Total Radiated Power

[13] In the numerical studies of several MTM-based structures conducted in section 4, a thorough investigation of their spatial near-field distributions will be undertaken. Aside from these near-field investigations, significant attention will also be devoted to the total radiated power, P_t, henceforth termed the total power. The total power is given by the expression

$$P_t = \lim_{r\to\infty} \frac{1}{2} \int_{\theta=0}^{\pi} \int_{\varphi=0}^{2\pi} \mathrm{Re}\left\{\vec{E}_t(r,\theta,\varphi) \times \vec{H}_t^*(r,\theta,\phi)\right\} \cdot d\vec{s}, \tag{11}$$

where * denotes the complex conjugate and $d\vec{s} = \hat{r}r^2 \sin\theta d\phi d\theta$ is the outward pointing surface differential element. In addition, $\vec{E}_t$ and $\vec{H}_t$ denote the total electric and magnetic field, respectively, in region 3. When the EHD is in region 3, these total fields are equal to the sum of the field generated by the EHD (1) defined for $r > r_s$ and the field (6c), while they equal the field (6c) when the EHD is located in either region 1 or 2. The expression for the total electric and magnetic fields in (11) is easily obtained by introducing the large argument expansions of the involved spherical Hankel functions [*Abramowitz and Stegun*, 1965, chapter 11]. The final expression for the total power then takes the form

$$P_t = \frac{2\pi}{\omega k_0} \sum_{n=1}^{\infty} \sum_{m=-n}^{n} \frac{n(n+1)}{2n+1} \frac{(n+|m|)!}{(n-|m|)!} \cdot \left[\frac{1}{\varepsilon_0} |\alpha_{nm}|^2 + \frac{1}{\mu_0} |\beta_{nm}|^2 \right], \quad (12)$$

where $\alpha_{nm} = a_{nm}^{(4)} + A_{4,nm}$, $\beta_{nm} = b_{nm}^{(4)} + B_{4,nm}$ if the EHD is located in region 3, and $\alpha_{nm} = A_{4,nm}$, $\beta_{nm} = + B_{4,nm}$ if the EHD is located in either region 1 or 2.

[14] The power radiated by the EHD when it is situated alone in free space is denoted by P_i and is given by (12) with $\alpha_{nm} = a_{nm}^{(4)}$ and $\beta_{nm} = b_{nm}^{(4)}$. However, the power radiated by the EHD in free space has a considerably simpler and well-known form if it is not expressed in terms of the spherical vector wave functions. In particular, with *Balanis* [1989, p. 137] one finds

$$P_i = \frac{\eta_0 \pi}{3} \left| \frac{p_s k_0}{2\pi} \right|^2. \quad (13)$$

Of particular interest to the present work is the comparison of the total power radiated in the presence of the concentric MTM spheres to that radiated by the EHD alone in free space. To this end, the quantity designated as the power ratio (PR) is introduced. It is given by

$$\mathrm{PR} = \frac{P_t}{P_i}, \quad (14)$$

with P_t and P_i given by (12) and (13), respectively. It is noted that we employ here an impressed Hertzian dipole as the source which corresponds to a constant current generator.

[15] It is noted that the PR in (14) is equivalent to the radiation resistance of the EHD radiating in the presence of the structure normalized by the radiation resistance of the EHD radiating in free space. However, the input impedance cannot be properly defined since the EHD is an idealized source. Thus the PR simply measures the relative performance of two idealized canonical configurations: the EHD with or without the MTM-based structure. In the consideration of realistic antennas, the issue of impedance matching the antenna to the source is profoundly important. We do not address this practical issue here since it has been considered by *Ziolkowski and Erentok* [2006]. Instead, we concentrate on the physical properties and responses of the canonical MTM-based systems in both their radiating and scattering configurations.

3. Resonance Condition: Discussion and Derivation

[16] Prior to presenting the results for specific electrically small structures, it is useful to derive the conditions for which they become resonant; i.e., they provide enhancements of the total power. Specific details on the derivation of these conditions have already been reported by, e.g., *Alú and Engheta* [2005], *Arslanagic et al.* [2006], and *Ziolkowski and Kipple* [2005] for cylindrical and spherical structures; thus, only the main points associated with the spherical structures are included below.

[17] With the objective of enlarging the total power in (12) and, hence, the PR in (14), the amplitudes of the coefficients $A_{4,nm}$ and/or $B_{4,nm}$ must be large. When the spheres are made of DPS materials only, these coefficients become large only when the sizes of the spheres are on the order of, or larger, than the wavelengths in the materials [*Engheta and Ziolkowski*, 2006, chapter 2]. These resonances are referred to as the wavelength-sized natural resonances of the structure [*Arslanagic et al.*, 2006]. As the size of the object becomes electrically small, these resonances are lost since the natural modes cannot exist below a certain cutoff size [*Engheta and Ziolkowski*, 2006, chapter 2]. In contrast to this, the coefficients may exhibit a resonance when the structure consists of specific combinations of DPS, DNG, and/or SNG materials, even if the structure is electrically small. This is due to the presence of the so-called subwavelength-sized natural resonances (also termed interface resonances by *Engheta and Ziolkowski* [2006, chapter 2] and *Alú and Engheta* [2005]) in such electrically small structures [see *Engheta and Ziolkowski*, 2006, chapter 2; *Alú and Engheta*, 2005; *Arslanagic et al.*, 2006; *Ziolkowski and Kipple*, 2005].

[18] In order to find the condition for which the amplitudes of $A_{4,nm}$ and $B_{4,nm}$ become large, it is first recalled that these coefficients are determined independently of each other. The TM coefficients $A_{4,nm}$ are proportional to the product of the inverse of the matrix $\bar{\bar{A}}_n$ and the first four elements of the excitation vector $\vec{\Psi}_{nm}$, i.e., $\Psi_{i,nm}$ with $i = 1$, 2, 3, and 4, while the TE coefficients $B_{4,nm}$ are proportional to the product of the inverse of the matrix $\bar{\bar{B}}_n$ and the last four elements of the excitation vector $\vec{\Psi}_{nm}$, $\Psi_{i,nm}$ with

$i = 5, 6, 7$, and 8. Then, in similitude with the procedure outlined in the work of *Arslanagic et al.* [2006] for the case of concentric MTM-based cylinders illuminated by an ELS, it is found that $A_{4,nm}$ and $B_{4,nm}$ become large when the magnitudes of the determinants of $\bar{\bar{A}}_n$ and $\bar{\bar{B}}_n$, respectively, attain a minimum. As the structures are electrically small, the small argument expansions of the functions in $\bar{\bar{A}}_n$ and $\bar{\bar{B}}_n$, which hold when the products $|k_1|r_1|k_2|r_1|k_2|r_2$, and $k_0 r_2$ are much smaller than unity, are used to derive the approximate analytical expressions for which the resonances will occur. The derivation of these resonance conditions is facilitated significantly by assuming that the materials in regions 1 and 2 are lossless. For the range of parameters to be investigated here, it can be shown that the TM coefficients $A_{4,nm}$ exhibit a resonance subject to the approximate condition

$$\frac{r_1}{r_2} \approx \sqrt[2n+1]{\frac{\{(n+1)\varepsilon_0 + n\varepsilon_2\}\{(n+1)\varepsilon_2 + n\varepsilon_1\}}{n(n+1)(\varepsilon_2 - \varepsilon_0)(\varepsilon_2 - \varepsilon_1)}}, \quad (15a)$$

while the TE coefficients $B_{4,nm}$ exhibit a resonance subject to the approximate condition

$$\frac{r_1}{r_2} \approx \sqrt[2n+1]{\frac{\{(n+1)\mu_0 + n\mu_2\}\{(n+1)\mu_2 + n\mu_1\}}{n(n+1)(\mu_2 - \mu_0)(\mu_2 - \mu_1)}}. \quad (15b)$$

[19] The conditions (15a) and (15b) are used to determine, for a given set of material parameters, the approximate ratio of r_1 and r_2 that will produce a resonant design. The condition for the electrically small resonant structure given by (15) depends on the mode number, n, the values of the permittivity and permeability of the three regions, and, most importantly, on the ratio of the inner and outer radii of region 2. The resonance condition therefore does not depend on the absolute size of these radii. A given resonant structure is defined on the basis of (15), e.g., by first selecting the material parameters and the mode number n that is to be excited as the dominant mode, and then selecting the inner (outer) radius. Subsequently, (15) gives the outer (inner) radius of the structure at which the resonance occurs. It is noted that certain small terms have been neglected in the derivation of (15). Thus, as will be demonstrated below, this condition only constitutes an approximation for the radii ratio at resonance and serves as a guideline to estimate the resonant configuration, i.e., as a starting point for the numerical analysis. Since it is implemented without the use of any small argument expansions, the numerical solution will, of course, be exact. The values of r_1 and r_2 so obtained will be the ones used to define the resonant structures that lead to the performance enhancements demonstrated below. It must be noted that relation (15) has also been derived by *Engheta and Ziolkowski* [2006, chapter 2] and *Alú and Engheta* [2005] for plane wave scattering from similar spherical structures. Furthermore, the condition (15a) for the $n = 1$ term has likewise been derived and discussed by *Kerker and Blatchford* [1982].

[20] As noted in the beginning of this section, large values of the total power and, hence, the PR may result if either $A_{4,nm}$ or $B_{4,nm}$ exhibit a resonance. In this regard, only (15b) or (15b), depending on the specific configuration, needs to be satisfied. According to *Engheta and Ziolkowski* [2006, chapter 2], and *Alú and Engheta* [2005], at least one of the parameters, ε_1 or ε_2 for (15a), and μ_1 or μ_2 for (15b), must be negative in order to satisfy the resonance conditions (15a) or (15b). In the work of *Kerker and Blatchford* [1982] it has also been pointed out that for (15a) with $n = 1$ the permittivities of regions 1 and 2 must have opposite signs to fulfill the condition. Thus, in this case, an ENG or MNG material, respectively, is needed in at least one of the regions 1 or 2. On the other hand, the simultaneous fulfillment of (15a) and (15b) requires either that at least one of the regions, 1 or 2, be a DNG material or that ENG-MNG or MNG-ENG structures be used. A resonance for the n'th mode in both the $A_{4,nm}$, and $B_{4,nm}$ coefficients requires ε_i and μ_i, $i = 1$ and 2, to be selected to ensure the same radii ratio n. As will be illustrated in section 6, the EHD-driven DPS-ENG structures may possess resonances similar to those exhibited by the DPS-DNG ones.

4. Numerical Results

4.1. Resonant Configurations: Definition

[21] The resonant configurations that have been selected to illustrate the results of interest are summarized in Table 2. Two different structures, namely those for which the dominant modes of radiation are the dipolar and the quadrupolar ones, are chosen.

[22] Regions 1 and 3 are assumed to be free space, while region 2 is taken to be a DNG medium. The positive material parameters in region 2 of the corresponding reference DPS-DPS structures are also included in the table. For these fixed materials and the specified value of the radius of region 1, the resonance conditions (15a) and (15b) were used to obtain the approximate value of the outer radius of region 2. These two structures are referred to as the dipolar and quadrupolar structures, respectively. Throughout the following discussion, the frequency of operation is $f_0 = 300$ MHz with the free-space wavelength $\lambda_0 = 1$ m. Although the outer radius of region 2 given in Table 2 is approximate, the forthcoming numerical investigations used the exact solution to determine the exact value of this radius. This exact value of the outer radius was subsequently used in the analysis of the relevant figures of merit.

Table 2. Material and Approximate Geometrical Parameters for Region 2 of the Electrically Small Resonant Dipolar and Quadrupolar Configurations

Structure	ε_2	μ_2	r_1	r_2
Dipolar	$\pm 3\varepsilon_0$	$\pm 3\mu_0$	10 mm = $\lambda_0/100$	18.57 mm = λ_0 / 53.85
Quadrupolar	$\pm 3\varepsilon_0$	$\pm 3\mu_0$	10 mm = $\lambda_0/100$	13.55 mm = λ_0 / 73.80

[23] The numerical results are illustrated for the following configuration. The EHD is taken to be z-oriented, i.e., $\hat{p}_s = \hat{z}$, and is located on the positive x-axis, i.e., with the coordinates (r_s, $\theta_s = 90°$, $\phi_s = 0°$), while the magnitude of the dipole moment is $p_s = 0.01$ Am. Thus, the structures under examination are either a DPS or a DNG spherical shell in the presence of a z-oriented EHD that is located at an arbitrary distance along the positive x-axis.

[24] It is noted that since the resonance condition in (15) is independent of the orientation of the EHD, behaviors similar to the results given below are expected for other orientations of the EHD. While they are not explicitly considered here, the results for such alternative EHD orientations can be obtained straightforwardly with the solution given here. Moreover, it is emphasized that the magnitude of the dipole moment is fixed, corresponding to a constant current source that is independent of the configuration. This is an impressed source without a feed network and, hence, the impedance matching of the radiating system to this source is not part of this investigation.

[25] It is furthermore noted, as observed from (15a), (15b) and Table 2, that for fixed material parameters, a considerably thinner structure is needed to excite the quadrupolar mode than the dipolar one. This behavior is similar to that found for the cylindrical structures treated by *Arslanagic et al.* [2006]. In addition, the diameter of the resonant dipolar structure is close to 37 mm, or $\lambda_0/25$ (which means $k_0 r_2 = 0.116$), while that of the quadrupolar structure is 27 mm, or $\lambda_0/37$ (which means $k_0 r_2 = 0.085$). Thus the structures considered here are indeed electrically small.

4.2. Electrically Small Dipolar Structures

[26] Presently, the electrically small resonant dipolar DPS-DNG structure is examined and compared to the corresponding DPS-DPS structure.

4.2.1. Total Power

[27] Figure 2 shows the PR as a function of the outer shell radius r_2 for the dipolar DPS-DNG and DPS-DPS structures when the inner radius is r_1 = 10 mm = $\lambda_0/100$ and the EHD is in region 1 at r_s = 5 mm = $\lambda_0/200$. As can be seen in Figure 2, a resonance in the PR with a maximum value PR $\approx$ 63 dB or PR $\approx 1.99 \times 10^6$ occurs for the DPS-DNG structure at r_2 = 18.69 mm = $\lambda_0/53.50$. This value is very close to the approximate value r_2 = 18.57 mm = $\lambda_0/53.85$ obtained from (15). In contrast, no resonance in the PR is found for the corresponding DPS-DPS structure; in fact, the PR is somewhat below 0 dB for all considered values of r_2. These results clearly show the advantage of the electrically small dipolar DPS-DNG structure over the corresponding DPS-DPS one. Similar results, not included here, have been obtained for the same structures when the EHD is located in regions 2 and 3. The peak at r_2 = 18.69 mm = $\lambda_0/53.50$ for the DPS-DNG structure is rather broad for this lossless and nondispersive case. Large PRs are obtained for a range of outer radius values, e.g., PR > 30 dB for $r_2 \in$ [18, 9.5] mm = [0.018, 0.0195] λ_0. Furthermore, it is of interest to note that the value of r_2 and the peak value of the PR at r_2 = 18.69 mm = $\lambda_0/53.50$ for the DPS-DNG structure agree very well with the corresponding peak value of the PR for the same radius reported by *Ziolkowski and Kipple* [2003], but for the EHD located at the center of the spheres.

[28] To investigate the effect of the EHD location on the enhancement of the total power, Figures 3a, 3b and 3c show, respectively, the PR as a function of the EHD location, r_s, when the EHD is located in regions 1, 2, and 3 for the DPS-DNG and DPS-DPS structures with r_1 = 10 mm = $\lambda_0/100$ and r_2 = 18.69 mm = $\lambda_0/53.50$. The location of the EHD varies in the interval $r_s \in$ [0.01, 9.99] mm = [0.00001, 0.00999] λ_0 for Figure 3a, in $r_s \in$ [10.1, 18.68] mm = [0.0101, 0.01868] λ_0 for Figure 3b, and in $r_s \in$ [18.7, 30] mm = [0.0187, 0.0300] λ_0 for Figure 3c.

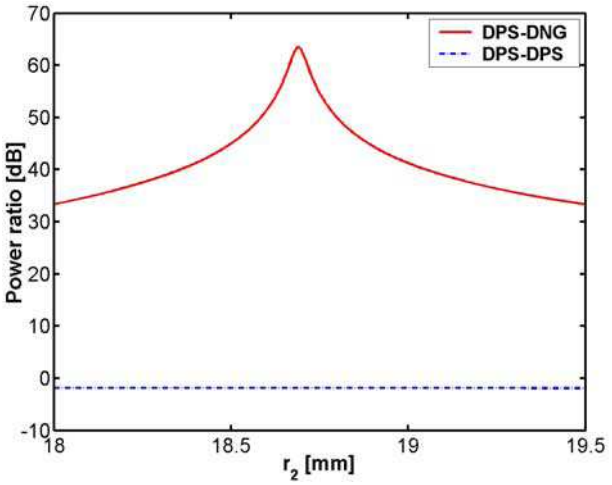

Figure 2. Power ratio as a function of the outer shell radius r_2 for the dipolar DPS-DNG and DPS-DPS structures. The EHD is in region 1 at r_s = 5 mm = $\lambda_0/200$.

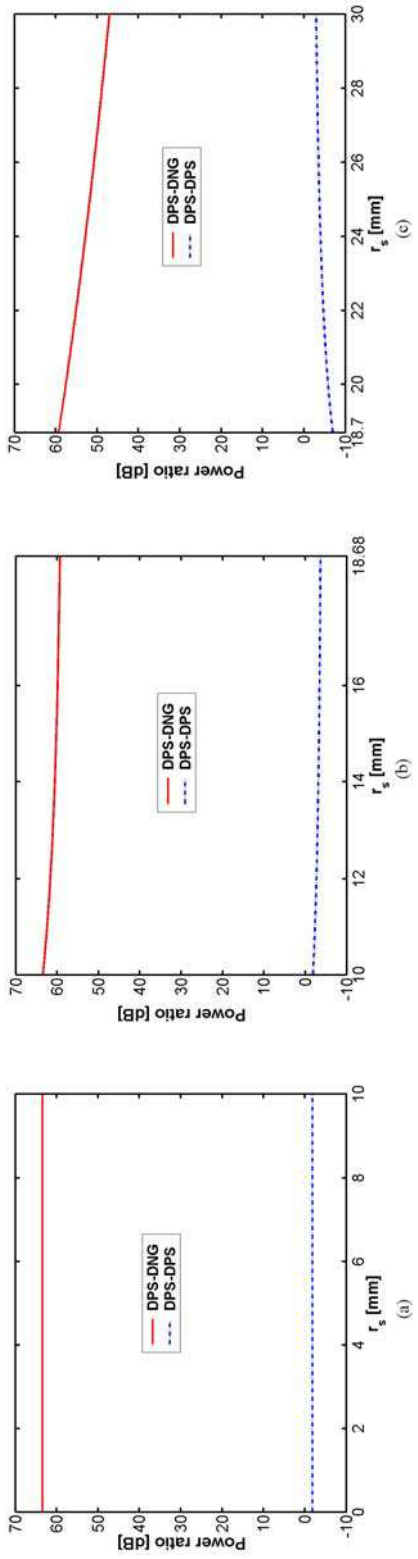

Figure 3. Power ratio as a function of the EHD location r_s for the dipolar DPS-DNG and DPS-DPS structures when the EHD is located in region 1 (a), region 2 (b), and region 3 (c).

[29] For all locations, the DPS-DPS structure gives no enhancement, while the corresponding DPS-DNG structure gives very large values of the PR. As the EHD moves through region 1, the PR is approximately constant and equal to PR $\approx$63 dB. As the EHD traverses region 2, a very small decrease of the PR is observed. For the case of the EHD in region 3, it is found that the PR values are diminished as the EHD is moved further away. However, for all of the considered EHD locations, significant enhancements of the total power are still in evidence.

[30] It is interesting to note that the largest PR values are obtained for EHD locations very close to the origin. One finds that the PR values are falling off slowly as the EHD moves away from the origin through regions 1, 2 and 3. However, the PR values in these three regions are not significantly affected by changing the EHD locations, this being particularly the case when the EHD is in regions 1 and 2. These findings are very interesting and are in sharp contrast to those obtained for the corresponding cylindrical structures excited by an electric line source. For those cylindrical cases the PR values vary significantly when the source is located in the different regions [*Arslanagic et al.*, 2006]. In particular, these cylindrical counterparts offer no enhancements when the source is located close to and at the origin, and at a specific location inside region 2, while the largest enhancements are found when the source is located near the interfaces of the cylindrical shell. The differences in the behavior of the spherical and cylindrical structures, as explained by *Arslanagic et al.* [2006], are caused by the fact that the latter allows the monopolar mode. The monopolar mode, which dominates for source locations close to and at the origin, and at a specific location inside region 2, produces no PR enhancements. As the source approaches the interfaces of the cylindrical MTM shell, the dipolar mode is emphasized strongly. As a consequence, large variations in the PR values for the corresponding cylindrical structures occur as the source location varies. In the spherical case, however, there is no monopolar mode regardless of the EHD location. The dipolar mode dominates the radiating/scattering processes when it is excited, and the corresponding enhancement is on the same order of magnitude for all of the considered EHD locations.

4.2.2. Near Field

[31] In order to investigate further the presence of the enhanced PR values when the EHD is radiating in the presence of the DPS-DNG structure, and their absence in the presence of the DPS-DPS structure, near-field investigations are performed next. For the near-field plots the quantity, 20 $\log_{10} |E_{t,\theta}|$, where $E_{t,\theta}$ is the θ-component of the total electric field normalized by 1V/m, is shown. The plane of observation is the xz-plane, and the field is shown in a circular region with a radius of 30 mm = λ_0/33.33.

[32] Figure 4a shows the near field of the EHD in free space; Figure 4b shows the near field of the DPS-DPS structure for which r_2 = 18.69 mm = λ_0/53.50 (curves representing the spherical surfaces of the DPS-DPS structure are also shown).

[33] The electric field in the near field of the EHD in free space would, of course, have a dipolar form in a coordinate system centered at the EHD. However, its θ-component is asymmetric due to the displacement of the EHD from the origin. On the other hand, the magnitude of the total electric field, although not shown here, is symmetric with respect to the displaced source location. Moreover, as expected, the θ-component appears to be more symmetric when the observation points are further from the origin where far-field conditions are reached. The near field in Figure 4b is very similar to the field in Figure 4a, implying that the present DPS-DPS structure does not affect the field of the EHD. Therefore, such a structure is not expected to lead to any enhancement of the total power, this being in line with the results presented in Figures 2 and 3. Similar results, not included here, have been obtained for DPS-DPS structures with the EHD located in any of the three regions.

[34] The θ-component of the electric field of the resonant dipolar DPS-DNG structure with r_2 = 18.69 mm = λ_0/53.50 is depicted in Figure 4c. It is clear from comparisons of Figures 4a–4c that the DNG structure has significantly affected the near field of the EHD. More specifically, the near field in Figure 4c has a dipolar form. This result indicates that an EHD in the presence of a DPS-DNG structure having these specific geometry and material parameters will excite a dominant dipolar mode. These results agree with those predicted by the approximate resonance conditions (15).

[35] An additional insight into the resonance behavior can be observed from Figure 4d where the total power spectrum of the n'th mode for this DPS-DNG structure is given. More specifically, the total power in the n'th mode, n = 1, 2 and 3, normalized by the total power in the dipolar mode (n = 1) is depicted. As observed, the vast majority of the total power is contained in the dipolar mode, while only a negligible amount is contained in the next two higher order modes. In particular, $P_t(n = 2)$ and $P_t(n = 3)$ are more than 80 dB below $P_t(n = 1)$, and essentially no power is contained in the $n > 3$ modes.

[36] Before closing this section, several remarks are in order. Although not included here, it was verified that the near field of the electrically small resonant dipolar DPS-DNG structure for other locations of the EHD in regions 1, 2, and 3 is very similar to the near field shown in Figure 4c. This implies that the excited resonant dipolar

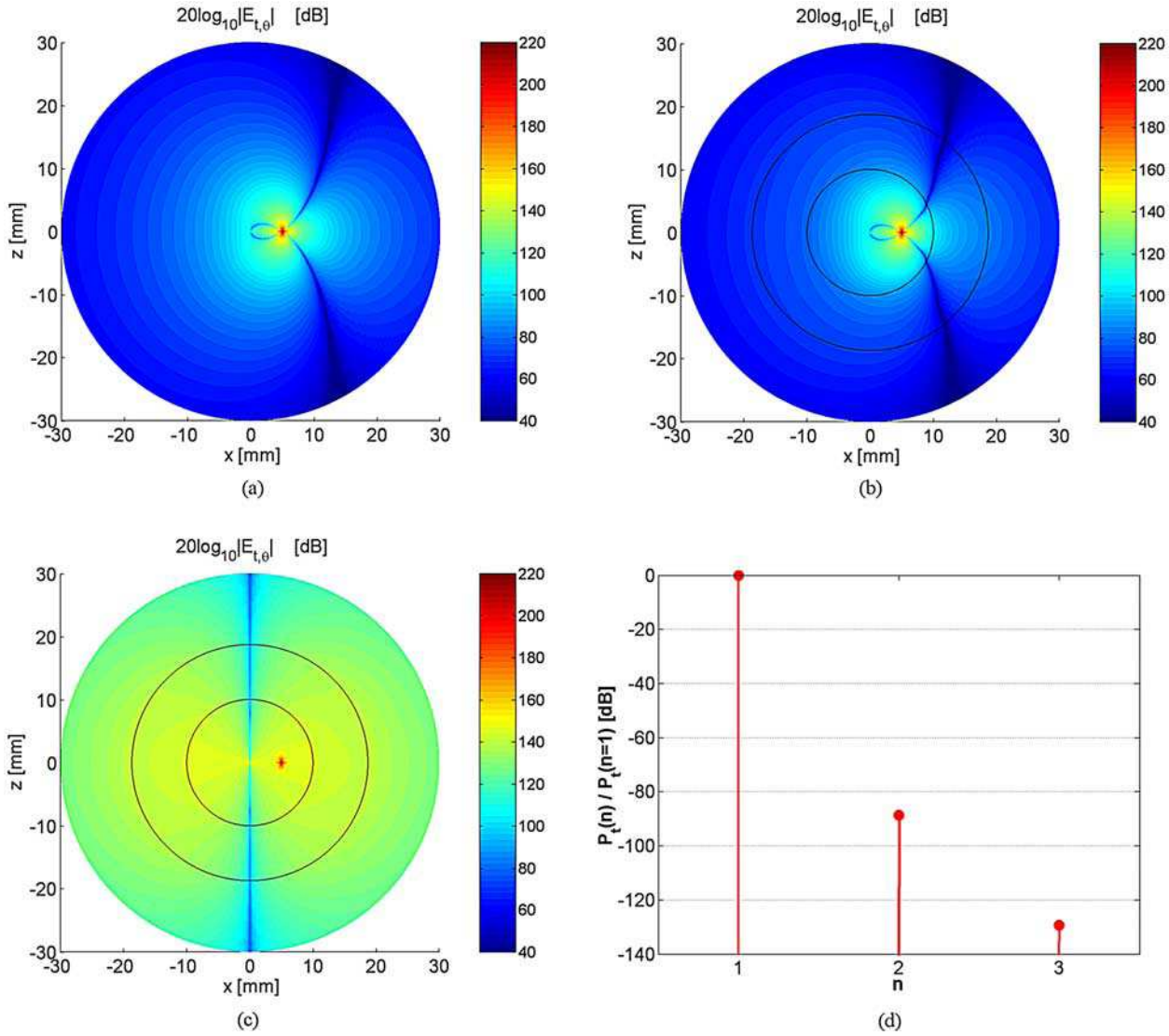

Figure 4. The magnitude of the θ-component of the electric near field of the EHD in free space (a), in the presence of the DPS-DPS structure (b), and in the presence of the resonant dipolar DPS-DNG structure (c). The EHD is in region 1 at r_s = 5 mm = $\lambda_0/200$. (d) The total power of the DPS-DNG structure contained in the n'th mode, n = 1, 2, and 3, normalized by the total power in the dipolar mode. The plane of observation is the xz-plane, and the field is shown in a circular region with a radius of 30 mm = $\lambda_0/33.33$.

mode is a natural dipolar mode of this structure. Consequently, the strongest (weakest) excitation of this mode is obtained by placing the EHD at locations where the field is a maximum (minimum). These findings are general and, therefore, also apply for the quadrupolar (and even higher order) structures considered next.

[37] The strength of the near field in Figure 4c is rather constant for those locations of the EHD used in the examination of the PR, see Figures 3 and 4c, i.e., along the positive x-axis throughout the three regions. Therefore, it is clear that the enhancements observed in Figure 3 are comparable in amplitude.

4.3. Electrically Small Quadrupolar Structures

[38] Next, the results for the quadrupolar DPS-DNG structures are illustrated and compared to the results of the corresponding DPS-DPS structures. Figure 5 shows the PR as a function of the outer shell radius r_2 for the

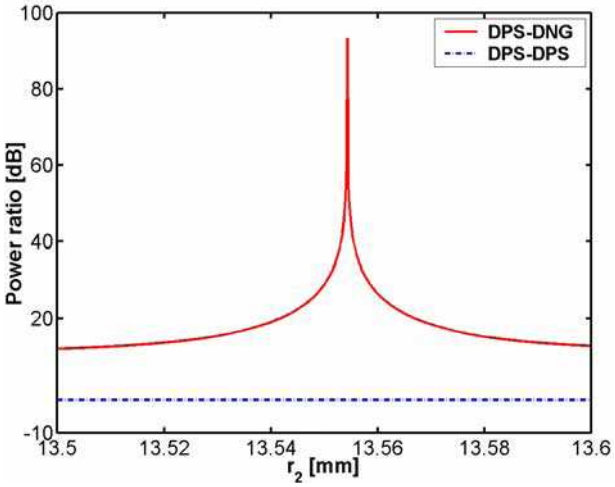

Figure 5. Power ratio as a function of the outer shell radius r_2 for the quadrupolar DPS-DNG and DPS-DPS structures when the EHD is located in region 1 at r_s = 5 mm = $\lambda_0/200$.

quadrupolar DPS-DNG and DPS-DPS quadrupolar structures having r_1 = 10 mm = $\lambda_0/100$ and for the EHD being located in region 1 at r_s = 5 mm = $\lambda_0/200$.

[39] As with the dipolar mode, the DPS-DPS structure does not offer any enhancements of the total power. On the other hand, a resonance peak and, thus, a significant enhancement of the total power is observed in Figure 5 for the DPS-DNG structure. The maximum PR of the DPS-DNG structure is approximately PR $\approx$ 93 dB at r_2 = 13.55 mm = $\lambda_0/73.80$ which agrees with the value in Table 2 predicted by the resonance condition (15). It is also found that the resonant enhancements reported in Figure 5 are larger, but extremely narrower than those occurring in the corresponding dipolar DPS-DNG structure. This difference between the dipolar and quadrupolar spherical structures is in line with the differences observed for the dipolar and quadrupolar cylindrical structures [*Arslanagic et al.*, 2006].

[40] To verify that these results are due to the resonant excitation of the quadrupolar mode, the near-field and the total power spectra of the n'th modes are again considered. The electric near field for the quadrupolar DPS-DNG structure for which r_2 = 13.55 mm = $\lambda_0/73.80$ is depicted in Figure 6a for the case where the EHD is located at r_s = 5 mm = $\lambda_0/200$ (curves representing the spherical surfaces of the DPS-DNG structure are also shown).

[41] Since the near field has a clear quadrupolar form, it follows that the EHD in the presence of this DPS-DNG structure excites the quadrupolar mode, and the enhancements of the total power result from this dominant mode. These findings are confirmed with the results given in Figure 6b, where the total power spectrum of the n'th mode, n = 1, 2, and 3, normalized by the total power in

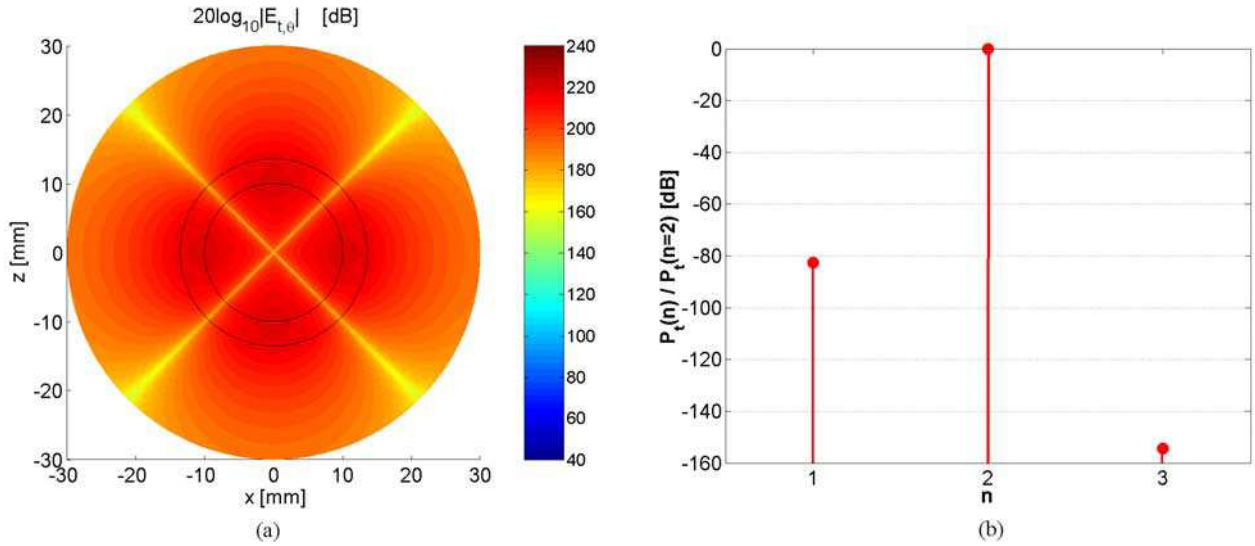

Figure 6. Quadrupolar DPS-DNG structure: (a) the magnitude of the θ-component of the electric near field when the EHD is in region 1 at r_s = 5 mm = $\lambda_0/200$, and (b) the total power in the n'th mode, n = 1, 2, and 3, normalized by the total power in the quadrupolar mode. In Figure 6a, the plane of observation is the xz-plane, and the field is shown in a circular region of radius 30 mm = $\lambda_0/33.33$.

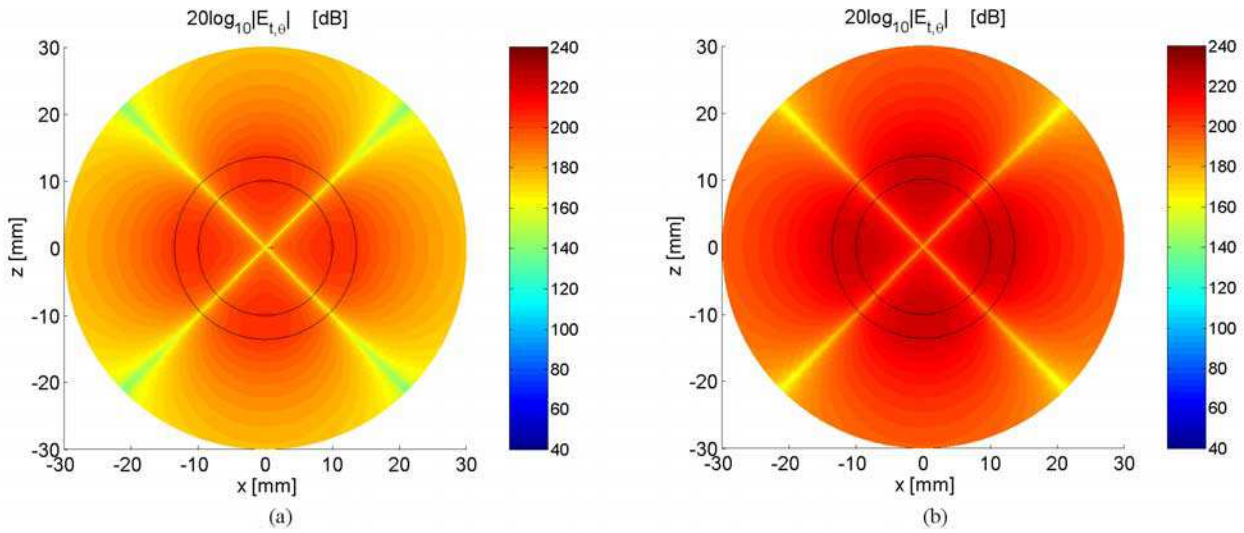

Figure 7. The magnitude of the θ-component of the electric near field of the DPS-DNG quadrupolar structure when the EHD is in region 1 at r_s = 1 mm = $\lambda 0/1000$ (a), and r_s = 9 mm = $\lambda_0/111.1$ (b).

the quadrupolar mode (n = 2), is shown. The largest part of the total power is contained in the quadrupolar mode, while only an extremely small amount is contained in the other modes. Again, essentially no total power is contained in the $n > 3$ modes. Results similar to those reported in Figure 6 are obtained for the quadrupolar DPS-DNG structure when the EHD is located in regions 2 and 3. One also notes from Figure 6a that this near field, evaluated at a given distance and direction, is larger (as the dynamic range is larger) than the near field of the corresponding dipolar structure depicted in Figure 4c. These differences in the near-field values for the dipolar and quadrupolar structures explain why the PR values are higher for the quadrupolar cases.

[42] Additional near-field results for the quadrupolar DPS-DNG structure are shown in Figures 7a and 7b for the EHD located at r_s = 1 mm = $\lambda_0/1000$ and r_s = 9 mm = $\lambda_0/111.1$, respectively. From these results and the one shown in Figure 6a, it is clear that once the resonant quadrupolar mode is excited, its form is rather unaffected of the location of the EHD. Thus, similar to the previously considered dipolar mode, the excited quadrupolar mode is a natural mode of the structure. As a consequence, placing the EHD at locations where the field is very small (large) leads to a weak (strong) excitation of this mode. With reference to Figures 6a and 7, the small field locations are, amongst others, near the origin. The locations of the largest fields are near the interfaces of the DNG shell along the x- and z-axes. Thus, the excitation of the resonant quadrupolar mode is very weak when the EHD is near the origin, while it is very strong when it is close to the interfaces of the DNG shell along the x- and z-axes.

[43] With these results in hand, it is next of interest to address the influence of the location of the EHD in the presence of a quadrupolar structure on the resonant enhancement of the total power. Figures 8a, 8b, and 8c show, respectively, the PR as a function of the EHD location, r_s, in regions 1, 2, and 3 for the DPS-DNG and DPS-DPS quadrupolar structures having the fixed radii: r_1 = 10 mm = $\lambda_0/100$ and r_2 = 13.55 mm = $\lambda_0/73.80$. The EHD location is varied through the interval $r_s \in$ [0.01, 9.99] mm = [0.00001, 0.00999] λ_0 in Figure 8a, $r_s \in$ [10.01, 13.54] mm = [0.01001, 0.01354]λ_0 in Figure 8b, and $r_s \in$ [13.56, 30] mm = [0.01356, 0.0300] λ_0 in Figure 8c.

[44] While no enhancements occur for the DPS-DPS structures, the DPS-DNG ones produce very large values of the PR for most of the considered EHD locations. Aside from the fact that the enhancements of the total power in the quadrupolar cases are larger than those for the dipolar cases for the majority of the EHD locations, the overall behavior of the results given in Figures 8b and 8c resembles that of the corresponding dipolar DPS-DNG structures. Nonetheless, there are some differences between the PR results in Figures 8a and 3a. In the former, the PR $\in$ [39.3, 99.3] dB when the EHD location traverses region 1 from the origin towards the DNG shell. This is in contrast to the dipolar DPS-DNG structure results given in Figure 3a, where the PR is nearly constant in this region. This behavior of the quadrupolar DPS-DNG structure is not surprising. One

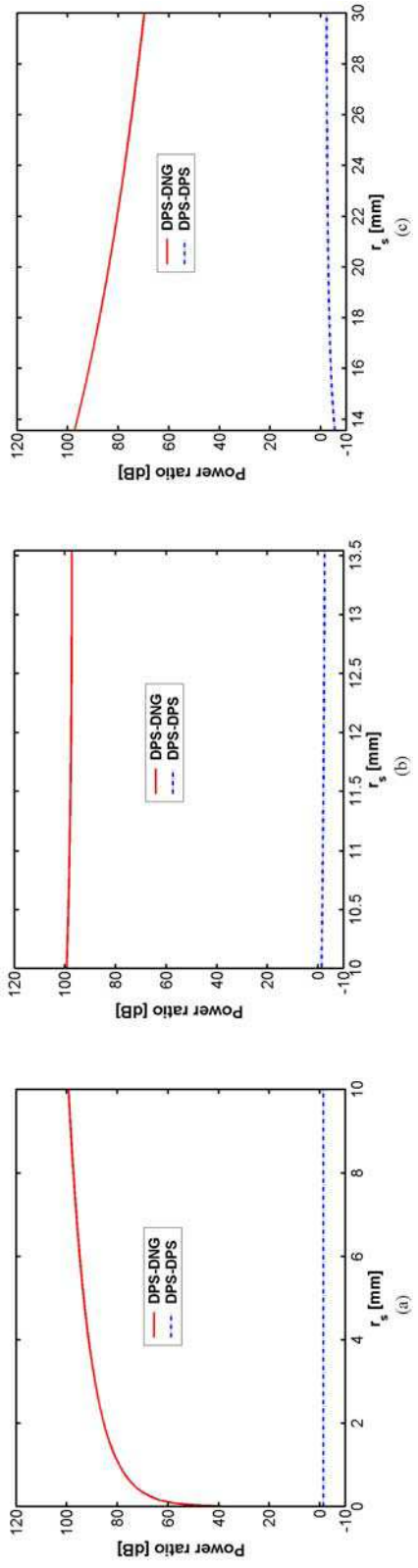

Figure 8. Power ratio as a function of the EHD location r_s for the quadrupolar DPS-DNG and DPS-DPS structures when the EHD is in region 1 (a), region 2 (b), and region 3 (c).

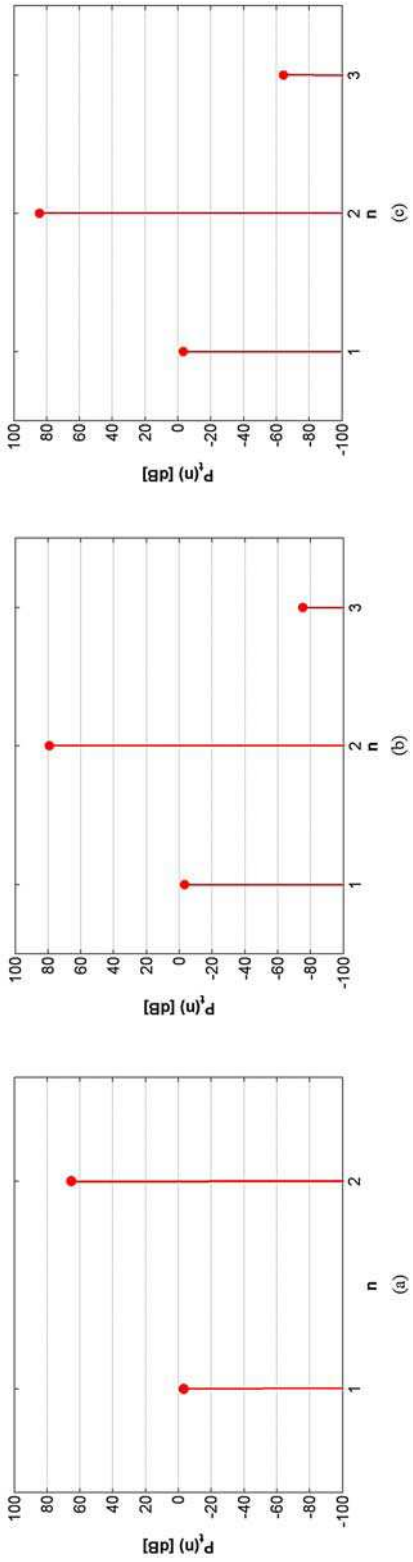

Figure 9. The total power contained in the n'th mode for the quadrupolar DPS-DNG structure when the EHD is located in region 1 at $r_s = 1$ mm = $\lambda_0/1000$ (a), $r_s = 5$ mm = $\lambda_0/200$ (b), and $r_s = 9$ mm = $\lambda_0/111.1$ (c).

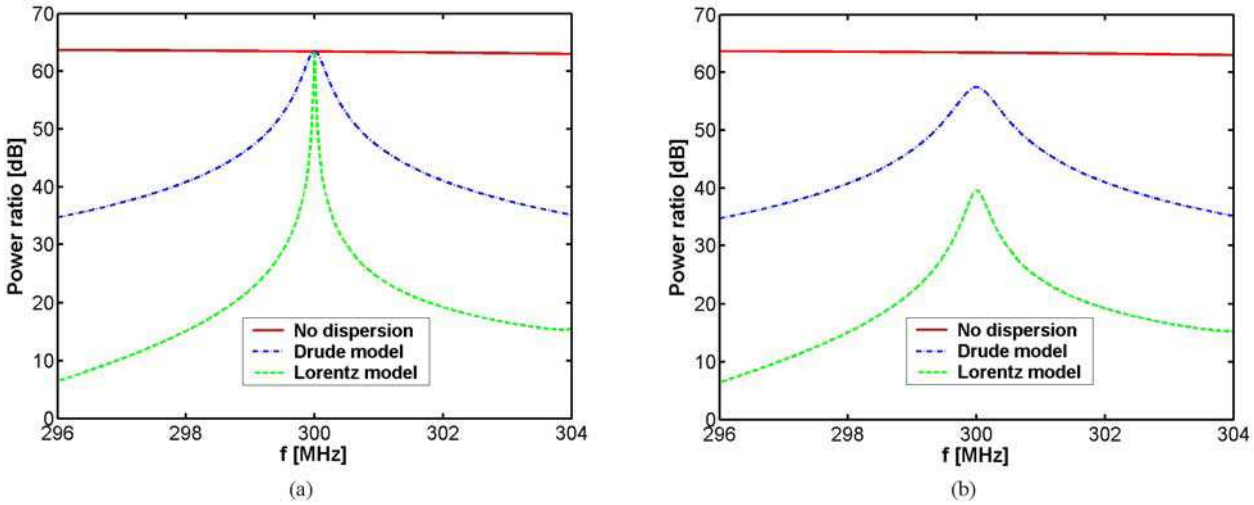

Figure 10. Power ratio as a function of the frequency for the dipolar DPS-DNG structure in which the DNG shell is described by nondispersive, Drude and Lorentz material models. The Drude and Lorentz dispersion models are lossless in (a) and lossy in (b). The EHD is located in region 1 at r_s = 5 mm = $\lambda_0/200$.

recalls that the resonant structure has been designed so that the EHD will dominantly excite the quadrupolar mode. Moreover, with reference to the above discussion on the near-field behavior and the characterization of the excited quadrupolar mode as the natural mode, it is recalled that this mode is excited most strongly (weakly) when the EHD is located near to the interfaces (origin) of the DNG shell. In particular, it is well known that only the dipolar mode exists at the origin [e.g., see *Ziolkowski and Kipple*, 2003; *Jones*, 1965, chapter 8]. As a consequence, the enhancements of the total power are diminished significantly as the EHD location is moved close to the origin; and they are completely absent when the EHD is located at the origin itself. On the other hand, they are significantly increased as the EHD approaches the surface of the DNG shell. This behavior is clarified further by the results shown in Figure 9, where the total power spectrum in the n'th mode, n = 1, 2, and 3, is shown for three representative locations of the EHD (note that in Figure 9a only the values for n = 1 and 2 modes are given since essentially no power is contained in the n > 2 modes). While the total power in the dipolar mode is almost constant in the three cases, an increase in the total power in the quadrupolar mode is noted as the location of the EHD changes from r_s = 1 mm = $\lambda_0/1000$ in Figure 9a to r_s = 9 mm = $\lambda_0/111.1$ in Figure 9c. Although not included here, it has been verified that at a distance of r_s = 0.0001 mm = $\lambda_0/10000000$, the total power in the quadrupolar mode is close to the total power in the dipolar mode. Thus, for such small distances from the origin, the quadrupolar configuration has no distinct advantage over the dipole case.

5. Effects of Dispersion and Losses

[45] Next, dispersion and losses are introduced in the DNG shell in order to examine their effects on the behavior of the resonant DPS-DNG structures considered in section 4. To this end, the well-known lossy Drude and Lorentz dispersion models of the permittivity and permeability are used. The lossy Drude models of the permittivity and permeability read

$$\varepsilon_2(\omega) = \varepsilon_0\left(1 - \frac{\omega_{pe}^2}{\omega(\omega - j\Gamma_e)}\right), \tag{16a}$$

$$\mu_2(\omega) = \mu_0\left(1 - \frac{\omega_{pm}^2}{\omega(\omega - j\Gamma_m)}\right), \tag{16b}$$

while the lossy Lorentz models take the form

$$\varepsilon_2(\omega) = \varepsilon_0\left(1 - \frac{\omega_{pe}^2}{\omega^2 - j\Gamma_e\omega - \omega_{er}^2}\right), \tag{17a}$$

$$\mu_2(\omega) = \mu_0\left(1 - \frac{\omega_{pm}^2}{\omega^2 - j\Gamma_m\omega - \omega_{mr}^2}\right). \tag{17b}$$

Table 3. Five Lossy Cases for the Additional Investigation on the Effects of Loss

Parameter	Case 1	Case 2	Case 3	Case 4	Case 5
$\varepsilon_2/\varepsilon_0 = \mu_2/\mu_0$	$-3 - j0.0003$	$-3 - j0.003$	$-3 - j0.03$	$-3 - j0.3$	$-3 - j3$
$LT_e = LT_m$	0.0001	0.001	0.01	0.1	1

[46] In (16) and (17), the quantities ω_{pe} and ω_{pm} represent the electric and magnetic plasma frequencies, Γ_e and Γ_m represent the electric and magnetic collision frequencies, while ω_{er} and ω_{mr} in (17) represent the resonance frequencies of the permittivity and permeability, respectively. The two models are designed to recover, at the angular frequency of operation, $\omega_0 = 2\pi f_0$ with $f_0 =$ 300 MHz the lossless permittivity and permeability values given in Table 2, which were used in section 4 to define the resonant DPS-DNG structures. For the Drude model, the values of ω_{pe}^2 and ω_{pe}^2 are determined from the real part of (16a) and (16b), respectively, evaluated at ω_o to recover the desired lossless material parameter values. For the Lorentz model, with the assumption that the losses are small, the frequency of operation f_0 must lie above the resonance frequency to obtain the required negative lossless material parameter values. Since the angular frequencies of the permittivity and permeability at resonance are given by $\omega_{er} = 2\pi f_{er} = \omega_{mr} = 2\pi f_{mr} = 2\pi f_r$, the frequency f_r is set to $f_r = 290$ MHz, and the values of ω_{pe}^2 and ω_{er}^2 for the Lorentz model are determined from the required values of the real parts of (17a) and (17b).

[47] To investigate the effects of the dispersion and loss, two specific cases are first considered. In the first case, $\Gamma_e = \Gamma_m = 0$ for both models, and in the second case, $\Gamma_e = \Gamma_m = 10^{-3}\ \omega_o$. Thus, the DNG shell is dispersive and lossless in the first case, while it is both dispersive and lossy in the second case. The influence of these two cases on the performance of the electrically small dipolar DPS-DNG structure with the EHD located in region 1 at $r_s = 5$ mm $= \lambda_0/200$ is shown in Figure 10. (The PR values given in this section are calculated for the same resonant dipolar configuration that was treated in section 4.2, with the exception that dispersion or/and loss are now included.) The results for the reference case, in which no dispersion occurs, are likewise included in the figure.

[48] As can be observed from Figure 10, the PR is almost constant in the depicted frequency range when the DNG shell is treated as lossless and nondispersive, and, hence, the response is broadband. In contrast to these nondispersive results, the bandwidth of the resonance attained at $f_0 = 300$ MHz is narrowed considerably when either of the two dispersion models is introduced into the DNG shell. Moreover, the Lorentz model results are characterized by an even narrower bandwidth than those obtained with the Drude model, this being particularly the case in the absence of losses as illustrated in Figure 10a. In the lossless dispersion cases it is important to note that the maxima of their PR values, which occur at the resonance frequency $f_0 = 300$ MHz, attain the same value as predicted for the nondispersive case. The inclusion of loss has two basic impacts on the PR values. With reference to Figure 10b it is first noted that the resonances remain at $f_0 = 300$ MHz, but they are broadened relative to the lossless cases. Secondly, the maxima of the PR values at the resonance frequency $f_0 =$ 300 MHz for the lossy dispersive models are lower than the nonlossy case value. In particular, the PR value at $f_0 =$ 300 MHz in the nonlossy case is 63.43 dB, while it is 57.44 dB for the lossy Drude dispersion model and 39.55 dB for the lossy Lorentz dispersion model. The difference in the PR behavior between the two dispersion models was expected. The Lorentz model, which has a faster frequency variation than the Drude model near the specified negative material values, has a much narrower bandwidth. The losses associated with the Lorentz model are also more severe (for the same collision frequencies) than those with the Drude model because the required negative values occur near its resonance frequency, where its losses are largest. In fact the values of the permittivity and the permeability in the lossy dispersion models evaluated at $f_0 = 300$ MHz are $\varepsilon_2 = \varepsilon_0\ (-3 - j0.004)$, $\mu_2 = \mu_0(-3 - j0.004)$ for the Drude model, and $\varepsilon_2 = \varepsilon_0\ (-3 - j0.0594)$, $\mu_2 = \mu_0(-3 - j0.059)$ for the Lorentz model. As a consequence, the electric and magnetic loss tangents at this frequency, denoted and given by $LT_e = \varepsilon_2''/|\varepsilon_2'|$ and $LT_m = \mu_2''/|\mu_2'|$, respectively, are $LT_e = LT_m = 0.0013$ for the Drude model and $LT_e = LT_m = 0.019$ for the Lorentz model. Thus, the loss in the Lorentz model is indeed larger than that in the Drude mode, even though their collision frequency values are the same. Similar results are obtained for the dipolar DPS-DNG structure when the EHD is located in regions 2 and 3.

[49] To further illustrate the effects of loss on the performance of the resonant dipolar DPS-DNG structure, several additional lossy, dispersionless cases were considered. In particular, five lossy cases whose permittivity and permeability values (at $f_0 = 300$ MHz) are shown in Table 3, along with the associated electric and magnetic loss tangent values, were chosen for the investigation. The real parts of the material parameters were fixed at

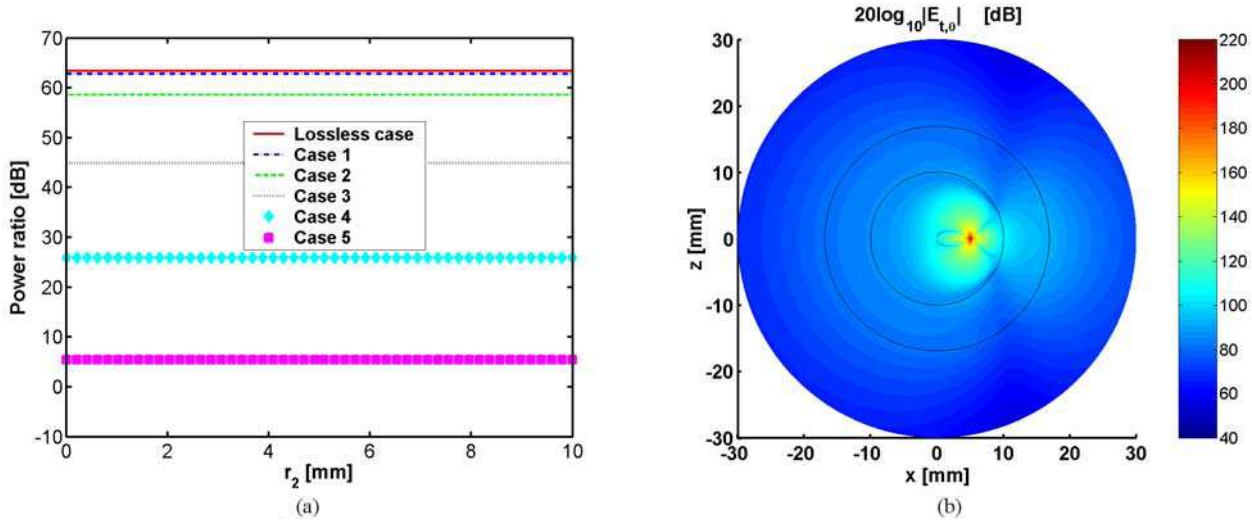

Figure 11. Impact of the DNG material losses: (a) Power ratio as a function of the EHD location, r_s, when the EHD is in region 1 for the lossless and the lossy (Cases 1-5) dipolar DPS-DNG structures. (b) The magnitude of the θ-component of the total electric near field of the dipolar DPS-DNG structure in which the DNG shell is modeled by Case 5 and the EHD is in region 1 at r_s = 5 mm = $\lambda_0/200$. In Figure 11b, the plane of observation is the *xz*-plane, and the field is shown in a circular region of radius 30 mm = $\lambda_0/33.33$.

the same value, while the amount of loss was varied from a very small to a very large value. In each of these cases, identical values of the relative permittivity and permeability were selected, thus yielding the same electric and magnetic loss tangents. The PR as a function of the EHD location, r_s, is shown in Figure 11a for these five lossy cases. The reference lossless case, treated in section 4.2, is likewise included for comparison purposes.

[50] While there is almost no difference between the lossless case and the very small loss Case 1, there is reduction of the PR in Case 2. As more loss is included in Cases 3 and 4, the PR values are lowered even further. They attain their lowest values for Case 5 when the largest amount of loss is included. One finds that an appreciable amount of loss in the DNG shell suppresses the excitation of the resonant dipolar mode. More loss further suppresses the interaction of the EHD with the DPS-DNG structure. Consequently, the inclusion of loss has the effect of lowering the enhancement of the total power. These observations are illustrated in Figure 11b, where the electric near field is given for the Case 5 lossy DPS-DNG structure when the EHD is in region 1 at r_s = 5 mm = $\lambda_0/200$. Comparing the results in Figure 11b with the electric near field for the EHD in free space given in Figure 4a, it is found that they are very similar, i.e., the Case 5 lossy DPS-DNG structure does not have any influence on the field radiated by the EHD, this being similar to the effect of the corresponding lossless DPS-DPS structure, see also Figure 4b. In other words, the Case 5 lossy DPS-DNG structure is at most only very weakly resonant and, therefore, it can not lead to any appreciable enhancement of the total power.

[51] It must be emphasized that only the results for the dipolar DPS-DNG structures have been presented in this section. Similar behavior is obtained when lossless and lossy dispersive quadrupolar, or even higher-order, DPS-DNG structures are considered. Although not included here, it has been shown that these higher-order structures have significantly narrower bandwidths and are, therefore, even more easily affected by the presence of dispersion and losses than the dipolar DPS-DNG structures are. These features observed for the concentric sphere geometry treated in this manuscript are also in evidence when the corresponding cylindrical structures are considered [see, e.g., *Arslanagic et al.*, 2006].

6. Wavelength-Sized Natural Resonances

[52] In the previous sections it was emphasized that DNG materials offer advantages over the usual DPS materials in the design of resonant electrically small MTM layered spheres, with significant enhancement of the total power. The existence of these resonances, despite the electrically small size, was attributed to the excitation of the necessary resonant mode, which was shown to be possible because of the presence of the DNG material. It will be demonstrated below that as the size of the structure is increased to be on the order of a

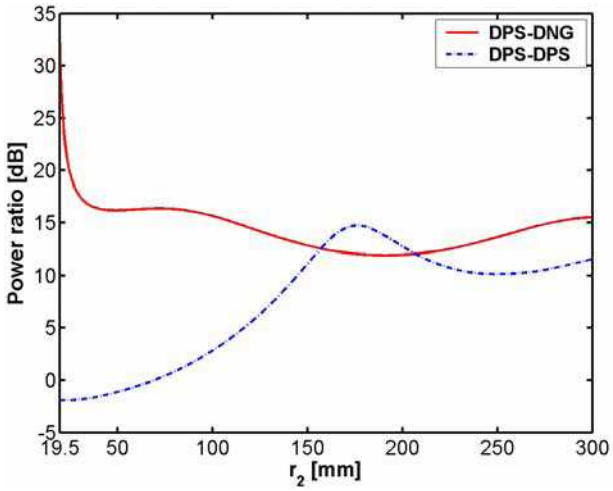

Figure 12. Power ratio as a function of the outer shell radius r_2 for the DPS-DNG and DPS-DPS spherical structures when the size of the structures is in the wavelength-sized natural resonance regime.

wavelength, the advantages of the DNG materials disappear, e.g., the same order of magnitude of the PR values are obtained for both DPS-DNG and DPS-DPS structures. This behavior is expected and occurs when the size of the structure enters the natural resonance regime; e.g., see *Engheta and Ziolkowski* [2006, chapter 2], *Alú and Engheta* [2005], and *Ziolkowski and Kipple* [2003] for detailed explanations.

[53] To illustrate this point, a DPS-DPS and a DPS-DNG structure with the material parameters given in Table 2 are considered. The frequency of operation is f_0 = 300 MHz and the location, as well as the orientation, of the EHD is the same as in section 4. The inner radius of region 2 is set to r_1 = 10 mm = $\lambda_0/100$, and the outer radius is allowed to vary in the interval $r_2 \in$ [19.5, 300] mm = [0.0195, 0.0300] λ_0 , corresponding to r_2 values much larger than those investigated previously. Figure 12 shows the PR values as a function of these r_2 values. For r_2 approximately greater than 150 mm = $\lambda_0/6.666$, comparable values of the PR are obtained in this wavelength-sized natural resonance regime for both the DPS-DPS and DPS-DNG structures. However, for the majority of the investigated r_2 values, the PR values for the DPS-DNG structure are slightly above those for the DPS-DPS structure. Nonetheless, none of the PR values in Figure 12 are on the order of the very large PRs obtained with the electrically small resonant dipolar, as well as quadrupolar structures, considered in section 4.

7. SNG Structures

[54] While the emphasis so far has been on the use of DNG versus DPS materials, it is possible, as noted in section 3, to use SNG materials to achieve subwavelength-sized natural resonances. More specifically, depending on the specific configuration under examina-

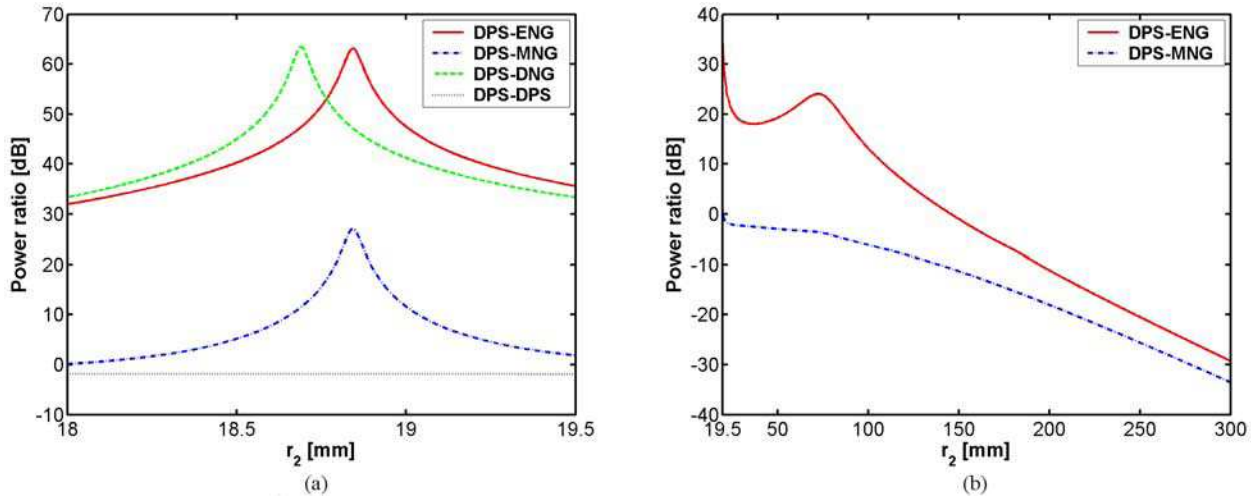

Figure 13. (a) Power ratio as a function of the outer shell radius r_2 for the electrically small dipolar DPS-ENG, DPS-MNG, DPS-DNG and DPS-DPS structures. (b) Power ratio as a function of the outer shell radius as it varies in the interval $r_2 \in$ [19.5, 300] mm = [0.0195, 0.0300] λ_0 for the DPS-ENG and DPS-MNG structures. In both Figures 13a and 13b, the EHD is in region 1 at r_s = 5 mm = $\lambda_0/200$.

tion, satisfaction of either of the two resonance conditions, i.e., (15a) or (15b), can still lead to electrically small resonant structures having the same enhancement properties as those discussed with the DPS-DNG structures. It is recalled that this occurs because the total power in (11) has resonant features when either $A_{4,nm}$ or $B_{4,nm}$ have resonant behaviors.

[55] To illustrate this behavior, it is useful to examine configurations consisting of an EHD radiating in the presence of a dipolar DPS-ENG structure and a dipolar DPS-MNG structure. These structures are chosen to have the same material and geometrical parameters as the dipolar DPS-DNG structure considered in section 4, except that for the DPS-ENG structure, the permeability in region 2 is positive and equal to $\mu_2 = 3\mu_0$ while for the DPS-MNG structure, the permittivity in region 2 is positive and equal to $\varepsilon_2 = 3\varepsilon_0$.

[56] Figure 13a shows the PR as a function of the outer radius r_2 for the dipolar DPS-ENG and DPS-MNG structures having the EHD located in region 1 at r_s = 5 mm = $\lambda_0/200$. The results reported in section 4 for the DPS-DNG and DPS-DPS structures are likewise included.

[57] The resonance peaks, at which significant enhancements of the total power are obtained, are found for the DPS-ENG and DPS-MNG structures at the same outer radius value r_2 = 18.84 mm = $\lambda_0/53.08$. These peaks clearly show that ENG or MNG materials may replace DNG materials in the task of generating resonances in electrically small MTM-based structures. These results are interesting and suggest that one might focus on obtaining appropriate SNG materials rather than DNG ones for this particular application. It is also interesting to note that the amplitude of the resonance peak for the DPS-ENG structure is PR $\approx$ 63 dB, and is thus identical to the peak value of PR obtained for the DPS-DNG structure in section 4.2. However, the peak PR value, PR $\approx$ 21 dB, for the resonant DPS-MNG structure is significantly lower than those obtained for the corresponding resonant DPS-ENG and DPS-ENG structures. Nonetheless, it is still considerably higher that the PR values generated by the DPS-DPS structures. These results reflect that the dominant field structure in the spherical vector wave expansions of the fields present in the electrically small cases is, as expected, TM. Thus, a DPS-ENG structure is favoured in the presence of an EHD. Note that if the source of electromagnetic radiation is a magnetic Hertzian dipole, the DPS-MNG structure would be naturally favoured, since the dominant term is TE in that case. It must be stressed that the underlying mechanism for the enhancement of the total power when an EHD radiates in the presence of DPS-ENG structures resembles that of the previously treated DPS-DNG structure. However, the resonant peaks for the two DPS-SNG cases, found at r_2 = 18.84 mm = $\lambda_0/53.08$, are attained at a somewhat larger value of the outer radius r_2 = 18.69 mm = $\lambda_0/53.50$, than for the DPS-DNG structure.

[58] For the SNG-based structures of larger size, the PR as a function of $r_2 \in$ [19.5,300] mm = [0.0195, 0.0300] λ_0 is shown in Figure 13b for both DPS-ENG and DPS-MNG structures. For the former, PR values above 10 dB are obtained up to the outer radius of r_2 = 100 mm = $\lambda_0/10$ mm, while beyond this radius the PR falls rapidly off. This is expected since the waves from the EHD cannot penetrate through an electrically large ENG shell in which the wave number is purely imaginary. This is also the case for the DPS-MNG structure, for which the blockage of the waves is emphasized at even smaller r_2 values and, thus, no enhancements are observed. As a consequence, the significant enhancements of the total power by use of DPS-ENG and DPS-MNG structures are only obtained if they are electrically small.

8. Summary and Conclusions

[59] In this paper the properties of the canonical configuration consisting of an arbitrarily oriented and located EHD radiating in the presence of a pair of concentric MTM spheres were investigated. An analytical solution in terms of spherical vector wave functions was first derived, and this was subsequently employed in a numerical investigation of electrically small, as well as large, MTM-based structures. The investigation is entirely theoretical since it assumes the existence of electrically small DNG materials and considers a canonical problem with an impressed current source. Nevertheless, the results reported here for the power ratio correspond to a normalized radiation resistance and are thus of relevance for the potential matching of generators to more realistic versions of these radiating systems. Particular emphasis was put on the electrically small dipolar and quadrupolar structures. In the numerical investigations, the near field spatial distribution and the total radiated power were examined. The results for the MTM-based designs were compared to the corresponding DPS-based designs.

[60] It was demonstrated that electrically small MTM-based structures, such as the DPS-DNG structures, can be designed to be resonant and thereby lead to significant changes of the field radiated by the EHD as well as significant enhancements of the total radiated power. These enhancements were found to be due to the so-called subwavelength-sized natural resonances of the MTM-based structures. Their existence was predicted analytically, and it was demonstrated that they do not exist for the corresponding DPS-DPS structures. It was also shown that changing the location of the EHD within the DPS-DNG structure had little impact on the total radiated power. This is in distinct contrast to the analogous cylindrically-shaped configurations [*Arslanagic et*

al., 2006]. Nonetheless, the spherical electrically small resonant quadrupolar DPS-DNG structure was found to exhibit some variation of the total radiated power with the EHD location. In particular, when the EHD is located near the center of the concentric spheres, the dipolar mode then dominates the interaction process. Thus, although such a resonant DPS-DNG structure was expected to excite the quadrupolar mode as the dominant one, it was found that other modes, such as the dipolar mode, could be excited for specific source locations. Moreover, it was found that the enhancements, although significantly narrower and more sensitive to variations of the material and geometrical parameters, are considerably larger for the quadrupolar structures than for the dipolar ones. This feature was also recognized with the corresponding cylindrical designs in the work of *Arslanagic et al.* [2006].

[61] The dispersive nature of the MTM material was shown to lead to a considerable narrowing in frequency of the resonances. Small and moderate losses did not make the resonances disappear but were found to lower the peak amplitudes of the resonant enhancements. However, the inclusion of very large losses did make the resonances disappear because of the suppression of the required resonant modes.

[62] Furthermore, it was demonstrated that ENG and MNG materials can offer results similar to those obtained with DNG materials. With the EHD, the exciting field is predominantly TM and for this case it was found that the DPS-ENG structure posses properties comparable to those of the DPS-DNG structure.

[63] It is important to emphasize that the electrically small resonant DPS-DNG structures investigated in this work give rise to a total radiated power comparable to and even exceeding those of electrically larger structures. For the latter, it was found that both DPS-DPS and DPS-DNG structures lead to resonant behaviors.

References

Abramowitz, M., and I. A. Stegun (1965), *Handbook of Mathematical Functions*, Dover, Mineola, N. Y.

Alú, A., and N. Engheta (2004), Guided modes in a waveguide filled with a pair of single-negative (SNG), double-negative (DNG) and/or double-positive (DPS) layers, *IEEE Trans. Microwave Theory Tech.*, *52*, 199–210.

Alú, A., and N. Engheta (2005), Polarizabilities and effective parameters for collections of spherical nano-particles formed by pairs of concentric double-negative (DNG), single-negative (SNG) and/or double-positive (DPS) metamaterial layers, *J. Appl. Phys.*, *97*, 094310.

Alú, A., F. Bilotti, N. Engheta, and L. Vegni (2007), Subwavelength, compact, resonant patch antennas loaded with metamaterials, *IEEE Trans. Antennas Propag.*, *55*, 13–25.

Arslanagic, S., R. W. Ziolkowski, and O. Breinbjerg (2006), Excitation of an electrically small metamaterial-coated cylinder by an arbitrarily located line source, *Microwave Opt. Technol. Lett.*, *48*, 2598–2605.

Balanis, C. A. (1989), *Advanced Engineering Electromagnetics*, John Wiley, Hoboken, N. J.

Caloz, C., and T. Itoh (Eds.) (2006), *Electromagnetic Metamaterials: Transmission Line Theory and Microwave Applications*, John Wiley, Hoboken, N. J.

Eleftheriades, G. V., and K. G. Balmain (Eds.) (2005), *Negative-Refraction Metamaterials: Fundamental Principles and Applications*, John Wiley, Hoboken, N. J.

Engheta, N. (2002), An idea for thin subwavelength cavity resonators using metamaterials with negative permittivity and permeability, *IEEE Antennas Wireless Propag. Lett.*, *1*, 10–13.

Engheta, N., and R. W. Ziolkowski (Eds.) (2006). *Metamaterials: Physics and Engineering Explorations*, John Wiley, Hoboken, N. J.

Jones, D. S. (1965), *The Theory of Electromagnetism*, Pergamon, Oxford.

Kerker, M., and C. G. Blatchford (1982), Elastic scattering, absorption, and surface-enhanced Raman scattering by concentric spheres comprised of a metallic and a dielectric region, *Phys. Rev. B*, *26*, 4052–4063.

Pendry, J. B. (2000), Negative refraction makes a perfect lens, *Phys. Rev. Lett.*, *85*, 3966–3969.

Stuart, H., and A. Pidwerbetsky (2006), Electrically small antenna elements using negative permittivity and permeability resonators, *IEEE Trans. Antennas Propag.*, *54*, 1644–1654.

Veselago, V. G. (1968), The electrodynamics of substances with simultaneously negative values of ε and μ, *Sov. Phys. Usp.*, *10*, 509–514.

Ziolkowski, R. W., and A. Erentok (2006), Metamaterial-based efficient electrically small antennas, *IEEE Trans. Antennas Propag.*, *54*, 2113–2130.

Ziolkowski, R. W., and A. Kipple (2003), Application of double negative metamaterials to increase the power radiated by electrically small antennas, *IEEE Trans. Antennas Propag.*, *51*, 2626–2640.

Ziolkowski, R. W., and A. Kipple (2005), Reciprocity between the effects of resonant scattering and enhanced radiated power by electrically small antennas in the presence of nested metamaterials shells, *Phys. Rev. E*, *72*, 036602.

S. Arslanagic and O. Breinbjerg, Ørsted·DTU, Electro-Science Section, Technical University of Denmark, Building 348, Ørsteds Plads, DK-2800 Kgs. Lyngby, Denmark. (sar@oersted.dtu.dk)

R. W. Ziolkowski, Department of Electrical and Computer Engineering, University of Arizona, 1230 E. Speedway Blvd., Tucson, AZ 85721-0104, USA.